

# Morphology modification of Si nanopillars under ion irradiation at elevated temperatures: plastic deformation and controlled thinning to 10 nm

Xiaomo Xu, Karl-Heinz Heinig, Wolfhard Möller, Hans-Jürgen Engelmann, Nico Klingner, Johannes von Borany and Gregor Hlawacek<sup>‡</sup>

Institute of Ion Beam Physics and Materials Research, Helmholtz-Zentrum Dresden-Rossendorf, Bautzner Landstrasse 400, 01328 Dresden, Germany

Ahmed Gharbi, Raluca Tiron

CEA-Leti, Rue des Martyrs 17, 38054 Grenoble, France

E-mail: [g.hlawacek@hzdr.de](mailto:g.hlawacek@hzdr.de)

2 October 2019

**Abstract.** Si nanopillars of less than 50 nm diameter have been irradiated in a helium ion microscope with a focused  $\text{Ne}^+$  beam. The morphological changes due to ion beam irradiation at room temperature and elevated temperatures have been studied with the transmission electron microscope. We found that the shape changes of the nanopillars depend on irradiation-induced amorphization and thermally driven dynamic annealing. While at room temperature, the nanopillars evolve to a conical shape due to ion-induced plastic deformation and viscous flow of amorphized Si, simultaneous dynamic annealing during the irradiation at elevated temperatures prevents amorphization which is necessary for the viscous flow. Above the critical temperature of ion-induced amorphization, a steady decrease of the diameter was observed as a result of the dominating forward sputtering process through the nanopillar sidewalls. Under these conditions the nanopillars can be thinned down to a diameter of  $\sim 10$  nm in a well-controlled manner. A deeper understanding of the pillar thinning process has been achieved by a comparison of experimental results with 3D computer simulations based on the binary collision approximation.

*Keywords:* helium ion microscopy, Monte Carlo simulation, sub-10 nm fabrication, ion beam damage, amorphization

Submitted to: *Semicond. Sci. Technol.*

## 1 Introduction

While the development of new device architectures and computing strategies should be disruptive to enable a rapid progress in the field, the underlying fabrication technology ideally builds upon existing knowledge to enable a quick and seamless transition to the new data processing regime. Examples for this approach towards the development of future computing units are new low power devices such as single electron transistors (SETs) or Si-based quantum computing strategies [1, 2]. The existing complementary metal oxide semiconductor (CMOS) technology can handle today’s demands on feature size and shape, but new architectures require new—ideally CMOS-compatible—fabrication processes to meet the upcoming challenges. Here, we present a CMOS-compatible ion beam based fabrication process for sub 15 nm pillars with the potential for gate-all-around (GAA) SET device architectures [3] and other similar technologies that require three dimensional building blocks with lateral length scales in the few-nm regime. We investigate the achievable diameter reduction for sub-50 nm pillars with a height of 70 nm and also propose a model for the ion beam based mechanism.

The interactions between ion beams and Si-based material systems have been extensively studied in the last decades due to the ubiquitous and manifold applications of ion beams for device fabrication. Examples include the doping of transistor active regions [4, 5] mostly using broad ion beams and milling of nanostructures [6, 7] using focused ion beams (FIBs). Side effects of ion beam processing of Si include defect accumulation and amorphization. Studies—mostly with unstructured bulk materials—to understand the mechanism and to avoid these effects have been carried out with various ion species, energy ranges, target structures etc. [8] and are comprehensively summarized in review papers [9, 10] and textbooks [11, 12].

Ion irradiation at elevated temperatures has been considered as a promising technique to mitigate ion beam induced damages and amorphization of the substrate during the irradiation processes [13–15]. For most semiconductors, a finite temperature  $T_c$ —lower than the temperature for epitaxial recrystallization [16, 17]§—exists at which amorphization is prevented during irradiation. This is related to out-diffusion of vacancies from the ion track region, and is described in the so called out-diffusion theory [18, 19]. According to this theory, at any finite temperature, a § for Si this is in the range of 550 °C to 600 °C

thermally driven dynamic annealing process, characterized by Si interstitial-vacancy recombination, competes with the amorphization caused by the incident ion. When the substrate temperature  $T \ll T_c$ , the ion damage prevails and Si undergoes continuous amorphization. Once the temperature exceeds  $T_c$  the dynamic annealing will recover the amorphized pocket of each incident ion, thus preventing the amorphization. The process is governed by ion mass, target temperature and—to a lesser extent—flux and ion energy. Here, we utilize this dynamic annealing process at slightly elevated temperatures to prevent the amorphization of nanostructures during ion beam irradiation.

In the case of the nanostructures used in this work the length scale of the ion collision cascade becomes comparable to the structure size which results in unanticipated effects. Such effects can arise from changes in the distribution of the deposited energy. These changes are a result of the truncation of the collision cascade by the nanostructure. This reduces the amount of energy deposited into the nanostructure and changes the distribution of the deposited energy as the final low particle energy part of the cascade is missing. However, this part is characterized by a high relative nuclear energy loss as compared to the part of the cascade closer to the impact point. In addition, new processes such as backside or forward sputtering can change the stability of the nanostructure during ion beam irradiation [20].

In this work we employ FIB and broad-beam irradiation in the few tens of keV range to shrink the diameter of few-tens of nm pillars down to nearly 10 nm. Specifically we use  $\text{Ne}^+$  irradiation at 25 keV under normal incident in a helium ion microscope (HIM) [21, 22]. In the HIM the sample is heated in-situ using a home-built heater stage that can be loaded through the load lock of the Carl Zeiss Orion NanoFAB. Although the HIM has a lateral resolution of less than 2 nm when using  $\text{Ne}^+$ , we scan the beam over a set of nanostructures to emulate a broad beam irradiation, to which we also compare the results at the end of the manuscript. The benefit of this approach is that a few pillars from the same sample chip can be irradiated at different fluences and/or at different temperatures. Possible morphological or structural changes can then directly be compared in the subsequent HIM imaging step at RT. This characterization has been performed using high resolution HIM and transmission electron microscopy (TEM) to obtain information on the morphology and crystallinity of the obtained nanopillars, respectively.

The recently developed Monte Carlo simulation program TRI3DYN [23] is used to perform a fully dynamic 3D simulation of the irradiation process. This is complemented

by sputter yields and distributions of sputtered particles extracted from the static collision simulation program TRI3DST [20, 24]. The simulated results are compared with experimental findings and help with the understanding of the underlying processes.

To demonstrate the possibility for upscaling of this method we also employ  $\text{Si}^+$  broad beam irradiation. Here, always the entire sample is irradiated and multiple samples have to be used to investigate the influence of temperature and ion fluence. Both local and broad beam based irradiation suggest a versatile and CMOS-compatible fabrication method of sub-10 nm diameter vertical Si nanostructures at slightly elevated but still CMOS-compatible temperatures.

## 2 Methods

Silicon nanopillars have been fabricated via patterning of Si-rich anti-reflective coating (SiARC) and spin-on carbon (SOC) hard mask with an electron beam direct write (EBDW) system (SB3054, VISTEC) and subsequent plasma dry etching (Centura<sup>®</sup>, Applied Materials) in the 200 mm production line at CEA-Leti. The half-height diameters of nanopillars range from 25 nm to 50 nm and the pitch is larger than 250 nm thus redeposition of sputtered atoms is prevented. The size of a nanopillar array is  $5\ \mu\text{m} \times 5\ \mu\text{m}$ .

The nanopillars are irradiated with a 25 keV focused  $\text{Ne}^+$  ion beam from the HIM. Scanning the beam over a small area of  $5\ \mu\text{m} \times 2\ \mu\text{m}$  with a sufficiently small pixel spacing and dwell time emulates the conditions in a broad-beam implanter. The beam current is restricted under 500 fA using a  $20\ \mu\text{m}$  Au aperture. Under this condition the time interval between two arriving Ne ions is longer than 320 ns compared to the typical lifetime of the collision cascade which is on the order of tens of ps, thus preventing temporal overlap of the collision cascades. To perform irradiations at elevated temperatures in the HIM a home-built heater stage with a tungsten filament capable of reaching  $\sim 500\ ^\circ\text{C}$  is employed. The temperatures of the sample and the stage are monitored with type K thermocouples. Unless noted otherwise the most important remaining HIM  $\text{Ne}^+$  irradiation conditions are: 1 nm pixel spacing and 0.1  $\mu\text{s}$  dwell time. Images of the nanopillars are taken using a 25 keV  $\text{He}^+$  beam at  $85^\circ$  tilt angle to sample surface normal with a probe size smaller than 0.5 nm. In addition, broad beam irradiation has been carried out using 50 keV  $\text{Si}^+$  from a 200 keV ion implanter (Danfysik Model 1090) at the Ion Beam Center (IBC) of the Helmholtz-

Zentrum Dresden-Rossendorf (HZDR)

Cross-sectional samples to analyse the lateral shape of selected Si nanopillars were obtained by FIB (Zeiss NVision 40) milling and lift-out of  $1\ \mu\text{m} \times 50\ \mu\text{m}$  TEM lamellae (about 50 nm in thickness). Images have been acquired with an FEI Titan 80–300 microscope using bright-field transmission electron microscopy (BF-TEM) with a contrast-enhancing objective aperture and energy-filtered transmission electron microscopy (EFTEM) using the plasmon-loss peak at 17 eV to show the contrast of Si abundance. These data allow to analyze the crystallinity of the nanopillars and the dimensions can be measured even when the pillar is amorphized. Nanopillar diameter and height, as well as the volume reconstruction for the sputter yield calculation were achieved with the help of software Fiji [25].

Monte-Carlo (MC) codes based on the binary collision approximation (BCA) have been employed to simulate the ballistic processes during ion irradiation in order to contribute to the interpretation of the experimentally observed phenomena. The static program TRI3DST [20, 26] models the irradiation of three-dimensional (3D) bodies whose surface can be described by analytical functionals. TRI3DYN [23, 24] is employed for fully 3D dynamic simulations of the modification of an irradiated structure during bombardment, with arbitrary bodies being set up in a 3D voxel grid. Both codes assume amorphous materials and do not include collective phenomena such as the viscous flow. Details of the simulations are given in the Supplementary Information.

### 3 Results and Discussions

#### 3.1 Amorphization of Si nanopillars

Selected silicon nanopillars are irradiated from the top at both room temperature (RT) and high temperature (HT) (400 °C) with 25 keV  $\text{Ne}^+$  using a fluence of  $2 \times 10^{16}\ \text{cm}^{-2}$ . HIM images recorded using an 85°-tilt of the non-irradiated, RT-irradiated and HT-irradiated nanopillars are shown in Figure 1(a)-(c), respectively. After the irradiation at RT, a strong change in shape of the nanopillars—characterized by a rounding of the upper edge accompanied by a severe loss of the height—can be observed. However, no such shape change is seen in the case of HT irradiation of the nanopillars.

In Fig. 1(d) identical nanopillars are irradiated with a combined RT and HT irradiation but in a different sequence. The resulting morphology can be compared in a qualitative way in the image. Both pillar fields have received the same total fluence but in

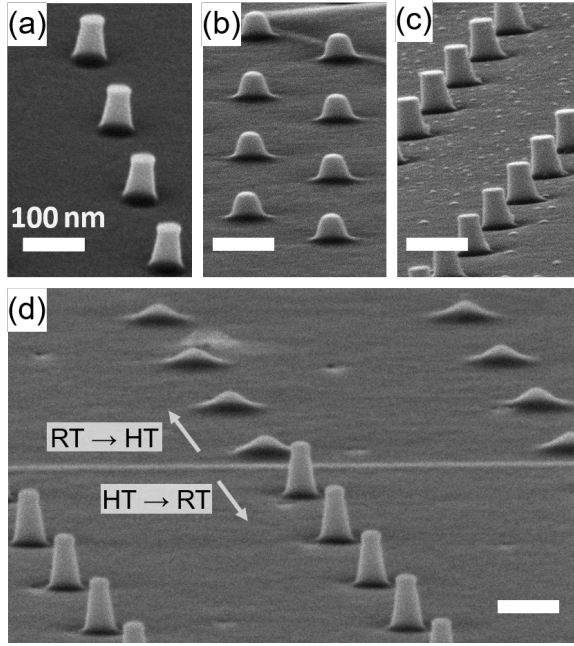


**Figure 1.** Si nanopillars with an original diameter of 25 nm have been irradiated with 25 keV  $\text{Ne}^+$  and subsequently imaged at  $85^\circ$  with  $\text{He}^+$  from a HIM. Image (a) shows the nanopillars before irradiation while (b) and (c) show the nanopillars after  $2 \times 10^{16} \text{ cm}^{-2}$   $\text{Ne}^+$  irradiation at RT and  $400^\circ\text{C}$ , respectively. Image (d) shows the direct comparison of nanopillars after having received  $2 \times 10^{15} \text{ cm}^{-2}$  at room-temperature and  $1.8 \times 10^{16} \text{ cm}^{-2}$  at  $400^\circ\text{C}$  but in different order. Scale bars in all images indicate 100 nm.

reverse orders. The pillar field in the back has first been irradiated at RT with a fluence of only  $2 \times 10^{15} \text{ cm}^{-2}$  followed by a fluence of  $18 \times 10^{15} \text{ cm}^{-2}$  at an elevated temperature of  $400^\circ\text{C}$ . The fluence of  $2 \times 10^{15} \text{ cm}^{-2}$  for the first irradiation step has been chosen so that it leads to an amorphization of the pillars. To ensure a complete amorphization of the pillars the chosen fluence is about 5 times higher than what has been reported for the amorphization of silicon by few 10 keV  $\text{Ne}^+$  irradiation [19]. However, the fluence is small enough to not lead to observable changes in the morphology of the pillars. The pillars in the foreground of Fig. 1(d) were first irradiated at  $400^\circ\text{C}$  with a fluence of  $18 \times 10^{15} \text{ cm}^{-2}$  followed by  $2 \times 10^{15} \text{ cm}^{-2}$  after being cooled down to RT. As a result both pillar fields have received a total fluence of  $2 \times 10^{16} \text{ cm}^{-2}$ . However, as is clear from Fig. 1(d) the sequence of RT vs. HT irradiation plays an important role for the final morphology. The amorphous pillars in the background—irradiated first at RT—are nearly completely removed. A closer look also reveals that the diameter at the foot of the former pillars has increased. The pillars in the foreground—irradiated first at HT—still show their pristine shape with nearly no observable change in morphology. The

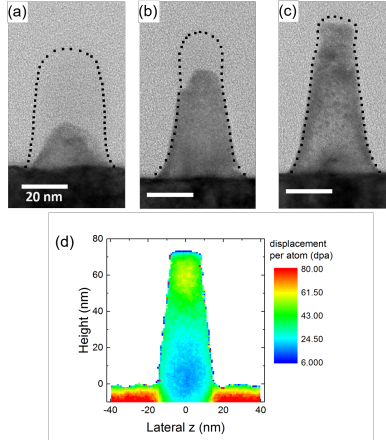


**Figure 2.** BF-TEM micrographs of Si nanopillars irradiated with  $2 \times 10^{16} \text{ cm}^{-2}$ , 25 keV  $\text{Ne}^+$  at (a) 250 °C, (b) 300 °C and (c) 350 °C showing the cases of the nanopillar being almost entirely amorphized, only top segment amorphized and entirely crystalline. The black dashed lines indicate the outlines of the actual Si nanopillars. (d) TRI3DYN simulation showing the distribution of displacements created by 25 keV  $\text{Ne}^+$  of  $2 \times 10^{16} \text{ cm}^{-2}$  fluence. The profile has to be compared to the extent of the crystalline and amorphous regions after an irradiation at temperatures lower than  $T_c$ .

final irradiation of the foreground pillars at RT ensures they receive the same amount of amorphization as the background pillars received initially. Again, this does not lead to a noticeable change of the pillar shape.

A detailed investigation of the temperature dependence of the ion beam induced amorphization is carried out on similar structures. A series of nanopillars is irradiated with  $\text{Ne}^+$  ions using a fluence of  $2 \times 10^{16} \text{ cm}^{-2}$  at various temperatures from 250 °C up to 350 °C in 25 °C steps. In Fig. 2(a)-(c) selected BF-TEM micrographs of typical structures are presented (TEM images for the other temperatures can be found in the supporting information). In BF-TEM micrographs only the crystalline part of the nanopillar is visible, and it is evident that after low temperature irradiation the pillar becomes amorphized. The black dashed lines in Fig. 2(a)-(c) outline the border of the actual pillar as extracted from corresponding EFTEM micrographs (not shown here; please see the supporting information for examples). With increasing irradiation temperature, at the same fluence an increasing part of the pillar stays crystalline and only a small part of the pillar becomes amorphous. Finally, for an irradiation temperature of 350 °C no amorphization can be detected from the BF-TEM images. From the investigation of the amorphization behaviour at additional temperatures (see the supporting information), we conclude that the critical temperature of amorphization ( $T_c$ ) during 25 keV  $\text{Ne}^+$  ion



irradiation for the presented Si nanopillars lies between 325 °C and 350 °C.

With the MC simulation program TRI3DYN, the dynamic evolution of a Si nanopillar under ion irradiation can be visualized. In Fig. 3(d) the accumulated displacements per atom (dpa) of the central slice of a nanopillar after 25 keV Ne<sup>+</sup> irradiation with a fluence of  $2 \times 10^{16} \text{ cm}^{-2}$  is shown. In this particular case, the comparison between the simulation and experiments is a simplification from the complex interplay leading to amorphization, including the original dpa created by the ion trajectory, temperature-dependent dynamic annealing, overlapping defect pockets as well as deformation due to viscous flow. BCA type MC simulation programs like TRI3DYN usually only treat amorphous samples, and effects such as dynamic annealing and viscous flow are not considered.

The obtained simulation results can well explain the amorphization profiles obtained by BF-TEM presented in Figs. 2(a,b). In these cases, only the top of the pillar is amorphized which corresponds to the region with the highest defect density according to the simulation result presented in Fig. 2(d). Furthermore, from the BF-TEM micrographs in Figs. 2(a,b) one can see that the interface between the amorphous and crystalline part of the Si nanopillar tends to bend towards the bottom of the pillar. This also agrees well with the simulated result which shows that in the lower part of the nanopillar the displacement density is higher close to the sidewalls than in the centre. This is attributed to the slightly tapered sidewall of the nanopillars (typically 7°) which leads to high angle sputtering, creating high amount of displacements close to the pillar surface. From the TRI3DYN result presented in Fig. 2 we conclude that a fluence of  $2 \times 10^{16} \text{ cm}^{-2}$  at RT results in a damage of at least 6 dpa. This is more than sufficient to amorphize the entire nanopillar in the absence of any dynamic annealing processes.

According to the defect out-diffusing model of amorphization [18], when the temperature of the crystalline silicon is higher than the amorphization critical temperature  $T_c$ , no matter how high the fluence is during an irradiation the originally crystalline structure will not be amorphized. From Figs. 1(c,d) and 2(c) one can see that during irradiation at temperatures higher than  $T_c$  the pillars stay crystalline and no morphological changes can be observed. This temperature of 325 °C to 350 °C is still 200 °C lower than the regime where epitaxial recrystallization could recover a large-area amorphous structure [16]. The nanopillars irradiated with 25 keV Ne<sup>+</sup> at RT become amorphous already after a very low fluence, similar to the amorphization fluence in bulk Si which is between  $1 \times 10^{15} \text{ cm}^{-2}$  and  $2 \times 10^{15} \text{ cm}^{-2}$  [19]. While the dynamic annealing

by the ion beam at HT above  $T_c$  is sufficient to prevent amorphization of the initially crystalline nanopillars, it can not recover the crystal structure of an initially amorphous nanopillar by epitaxial recrystallization. As a consequence, surface tension induced by ion irradiation leads to viscous behavior of amorphized nanostructures and the resulting plastic deformation visible in Fig. 1(b) and in the back of Fig. 1(d), as shown in previous studies—albeit mainly at ion energies from 100 keV to a few MeV—with various ion species, energies and target materials [27–29].

To summarize, we showed that above the critical temperature of amorphization  $T_c$  dynamic annealing prevents the amorphization of the crystalline Si nanopillars. From the TEM analysis we find out that this temperature corresponds to 325 °C to 350 °C for irradiation with 25 keV  $\text{Ne}^+$ . This is in agreement with the results from HIM imaging where we find severe deformation of initially crystalline nanopillars only after irradiation at temperatures below  $T_c$ . This deformation is a result of viscous flow of the amorphous material due to capillary forces acting on the nanoscale pillars. Initially amorphous pillars experience dramatic shape changes even if irradiated at HT, as the temperature for epitaxial recrystallization is still 200 °C higher and dynamic annealing is not sufficient to recrystallize the nanopillars.

### 3.2 Thinning of the nanopillars

Si nanopillars were irradiated at a temperature well above  $T_c$  to fully exclude the influence of ion-induced amorphization, and the applied fluence has been increased up to  $8 \times 10^{16} \text{ cm}^{-2}$ . The nanopillars studied here have a diameter at half-height of 47 nm and height of 71 nm. After the irradiation, the sample was immediately imaged with the HIM at a tilt angle of 85°. In Fig 3(a) the height and diameter of the nanopillars with the same original diameter after different irradiation fluences are plotted. With the increase of the fluence, a steady decrease of the diameter has been observed while the height remains almost unchanged. Linear fitting of the diameter reduction shows a slope, i.e. the reduction rate of  $-3.3 \pm 0.1 \text{ nm}/(1 \times 10^{16} \text{ cm}^{-2})$ . In the same diagram the simulated results of the thinning process from the program TRI3DYN are shown. Snapshots of the central 3 nm slice of the nanopillar after different irradiation fluences are presented in Fig. 3(b). While the simulation qualitatively fits with the experimental data it slightly overestimates the sputter yield for smaller diameters. Such a tendency was also observed in previous work [29] where the ion irradiation was performed at 45° incidence relative to the axis of a Si nanowire. The smaller the pillar diameter is, or

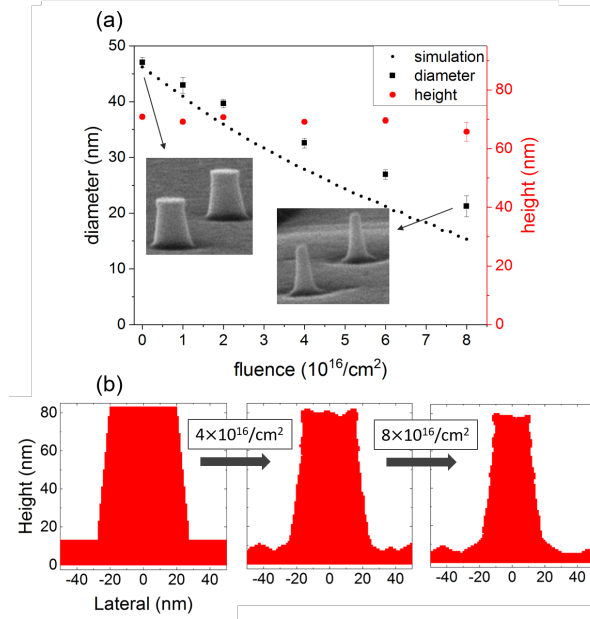


**Figure 3.** (a) Si nanopillar irradiated at  $400^\circ\text{C}$  with fluence up to  $8 \times 10^{16} \text{ cm}^{-2}$  shows a steady decrease of diameter without noticeable shrinkage of height. The nanopillars before and after irradiation are imaged with HIM at  $85^\circ$  tilt angle and shown as insets. The thinning process is also simulated with TRI3DYN and the diameter is plotted as an comparison to the experimental results. (b) Evolution of the central 3 nm slice of the simulated nanopillars during the  $\text{Ne}^+$  thinning process. The diameters at half-height are plotted in (a) showing good agreement compared to the experimental results.

when the ion impact position is close to the nanopillar rim, the higher the chance will be that a recoiled atom will leave the structure with a high kinetic energy. This reduces the energy deposited inside the pillar and subsequently leads to less energy deposited per incident ion as compared to a larger diameter pillar or a bulk system.

To further analyze the mechanism of the decrease of the nanopillar diameter, the average sputter yield during the pillar thinning process has been measured using the incident ion current and the lateral dimensions of the pillars and plotted against the diameter of the pillars. Detailed description of calculating the sputter yield from TEM micrographs is included in the Supporting Materials. As shown in Fig. 4(a), the average sputter yield is approximately constant as long as the diameter of the nanopillars is significantly larger than the lateral range of the  $\text{Ne}^+$  ions of  $\sim 19 \text{ nm}$ . The sputter yield measured for the nanopillars is at least 3 times higher than what is expected for sputtering at normal incidence on bulk Si surfaces as obtained from TRI3DST or SRIM.

Two factors are contributing to such a high sputter yield. First, due to the approximately  $7^\circ$  tapering, the sidewalls of the nanopillar are also exposed to the

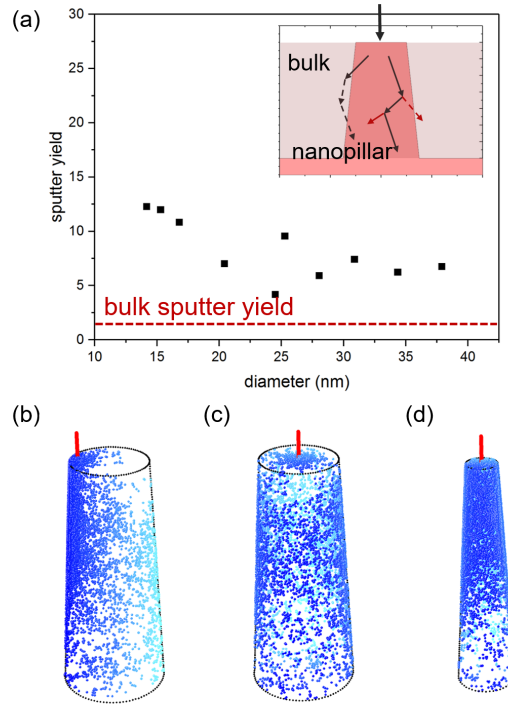


**Figure 4.** (a) Experimentally obtained sputter yield for 25 keV  $\text{Ne}^+$  in Si nanopillars plotted against the diameters at half height of the nanopillars. Due to enhanced forward sputtering the sputter yield in nanopillars is at least 3 times higher than the sputter yield in the bulk. (b)-(d) TRI3DST simulations showing profiles of surface sputtering events enhanced forward when an incident ion is (b) close to the pillar rim, (c) in the centre of the pillar or (d) when the pillar diameter is comparable with the size of the collision cascade. The diameters of the nanopillars in (b)-(d) are 30 nm, 30 nm and 15 nm, respectively. The colour coding (from dark blue to light blue) indicates the position of a sputtering event in the horizontal direction.

irradiation at a high glancing angle which results in a strongly enhanced sputter yield. This contribution is hard to quantify due to the additional radial curvature of the nanopillar sidewall. The second contribution comes from is the forward sputtering from ions hitting at normal incidence on the top of the nanopillar. From the schematic presented as an inset in Figure 4(a) one can see that in contrast to the case of a bulk structure (indicated as light red) where the collision cascade is fully embedded inside the sample, in the case of a nanopillar, the lateral extent of the collision cascade has a high probability to overlap with the surface. When a recoiled atom has a kinetic energy higher than the surface binding energy for Si of 4.7 eV [20], it will leave the nanopillar as a forward sputtered atom. Detailed analysis from the simulation results in Fig. 3(b) shows that at the initial diameter approximately 74% of the sputtering can be attributed to the forward sputtering from the ions penetrating into the top of the

nanopillar.

As the irradiation proceeds, the two contributions evolve in different manners. The high-angle sputtering on the sidewalls of the nanopillars slightly decreases with the decreasing diameter and unchanged sidewall tapering (see Fig. 3(b) and the insets in Fig. 3(a)). On the other hand, forward sputtering from ions hitting the top of the pillar will be more severe due to a larger surface to volume ratio.

Results from simulations, using TRI3DST, of focused-beam irradiation onto a Si nanopillar are shown in Fig. 4(b)-(d). The ions hit the top surface of the nanopillar at (b) 5 nm from the rim and (c)-(d) in the centre. For statistical reasons, an incidence of 1000 ions was simulated in all cases. In Fig. 4(b)-(d), blue dots indicate the position on the nanopillar sidewall where a sputter event occurred. It is clear that for every single incident ion, the smaller the diameter of the nanopillar is, or the closer the incident spot is located to the rim, the higher the amount of sputtered atoms will be. This behavior results in a steady decrease of the nanopillar diameter, mostly due to the enhanced forward sputtering. In this model, two distinctive stages will be observed for such a thinning process. When the diameter of the nanopillars is significantly larger than the lateral range of the collision cascade, the incident ions that create forward sputtering near the rim, such as in the case of Fig. 4(b), are unlikely to sputter from the other side of the nanopillar. Incident ions closer to the centre of the nanopillar, as shown in Fig. 4(c), would only induce a small amount of forward sputtering as the collision cascade barely reaches the pillar surface. As a consequence, the decrease of the pillar diameter has a linear dependency on the fluence. When the diameter of the nanopillars is comparable to or smaller than the size of the collision cascade, which is 18.6 nm in the case of 25 keV  $\text{Ne}^+$ , the chance that a recoil atom leaves the nanopillar via forward sputtering is high, independent from the ion impact position.

However, with decreasing pillar diameter, the size and shape of the collision cascade will also change. This is due to the limited size of the nanopillar, which reduces the actual average lateral range of the ions to a value smaller than the diameter but also reduces the range of the ions as they are more likely to leave the target structure. This situation is depicted in the inset of Fig. 4(a). The lower part of the bulk collisions cascade is missing in the collision cascade inside the nanopillar. This also result in a redistribution of the energy deposition and the related defect density. In the nanopillar more energy is deposited close to the top which leads to more sputtering at the top and eventually a reduction of the pillar height.

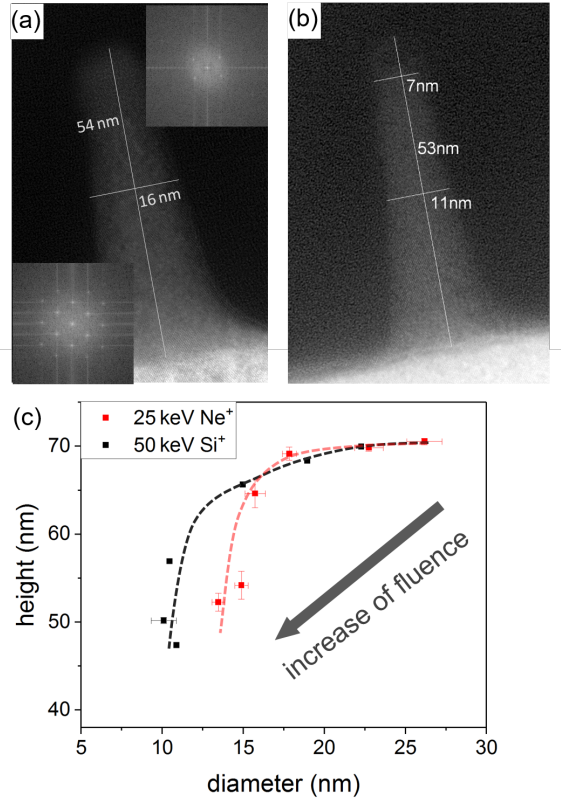


**Figure 5.** EFTEM micrographs show the nanopillars after HT-irradiation with (a)Ne<sup>+</sup> and (b)Si<sup>+</sup> of  $6 \times 10^{16} \text{ cm}^{-2}$  fluence. Fast Fourier transform (FFT) shows in both cases the top segment of the nanopillar is partially amorphized while the lower part remains crystalline. (c) As measured from 85°-tilted HIM and EFTEM images, the thinning from Ne<sup>+</sup> in Si nanopillars is limited when the diameter gets smaller than 16 nm while using Si<sup>+</sup> for the same purpose could reduce the diameter to 11 nm.

To demonstrate the potential for upscaling to industrial applications, we also performed Si<sup>+</sup> broad beam irradiation of nanopillar arrays in a standard ion implanter. To be able to compare the results to the previous Ne<sup>+</sup> irradiation, we used 50 keV Si<sup>+</sup>, which has the similar dpa as 25 keV Ne<sup>+</sup>, to irradiate the nanopillars at 400 °C. In Fig. 5(a) and (b) EFTEM micrographs of nanopillars after a fluence of  $6 \times 10^{16} \text{ cm}^{-2}$  with focused Ne<sup>+</sup> and broad-beam Si<sup>+</sup> are shown. These experimental conditions were chosen as they represent the highest fluences applied in both irradiation conditions that do not lead to a strong decrease of the nanopillar height. Both cases indicate the experimental limit for possible lateral pillar shrinking. Fast Fourier transform (FFT) results of the upper and lower part of an irradiated nanopillar are shown as insets in Fig. 5(a). They reveal that while the lower part of the Si nanopillar remains single crystalline the top part is characterized by a co-existence of crystalline and amorphous areas. As we further increase the irradiation fluence, the height of the nanopillar start to

decrease and the interface between the crystalline and amorphous parts moves towards the bottom. In the case of Si nanopillars irradiated with  $\text{Si}^+$  of  $6 \times 10^{16} \text{ cm}^{-2}$  fluence, the majority of the nanopillar also remains crystalline despite the higher density of defects in the vicinity of the top surface, indicating a better structural integrity than the one irradiated with  $\text{Ne}^+$ .

In Figure 5(c) the average height and diameter of the nanopillars during the thinning processes via focused  $\text{Ne}^+$  and broad-beam  $\text{Si}^+$  are plotted. The dashed lines are guides to the eyes to allow a clear comparison of the trends between irradiation with the two ion species. In the case of  $\text{Si}^+$  irradiated nanopillars, the diameter was measured via 85°-tilted HIM imaging subtracting the thickness of native oxide on the nanopillar sidewalls. While in both cases the curves eventually turn steep as the height starts to decrease and the thinning process slows down, allowing for a 15 % reduction of height, the achievable diameters for  $\text{Ne}^+$  and  $\text{Si}^+$  thinned nanopillars are 14 nm and 11 nm, respectively.

The difference in final diameter may be attributed to the following factors. First, with the projected ranges  $R_p$  of 73.2 nm for 50 keV  $\text{Si}^+$  and 56.9 nm for 25 keV  $\text{Ne}^+$ , the  $\text{Si}^+$  better fits the height of the original nanopillars. A higher energy of the incident ion would result in a deeper and shallower energy deposition thus postponing the defect accumulation at the top segment of the nanopillars. Second, Si self-irradiation leads to a more forward directed collision cascade due the optimal energy transfer between the incident Si and the target Si atoms having the same mass. As a consequence Si irradiation results in more homogeneous sputtering of the pillar and a slower reduction of the longitudinal range due cascade truncation by the pillar.

## 4 Conclusion

In this work, nanopillars with diameters of 50 nm and below were irradiated with  $\text{Ne}^+$  from a helium ion microscope at temperatures between 250 °C and 400 °C. The critical temperature of amorphization under ion beam irradiation  $T_c$  was found in the range between 325 °C and 350 °C. The morphology of the Si nanopillars evolves accordingly at different temperatures during  $\text{Ne}^+$  irradiation. At temperatures lower than  $T_c$ , the nanopillar shape turned conical and a strong decrease in height occurred due to the presence of viscous flow. When irradiated at temperatures higher than  $T_c$ , the Si nanopillars remained crystalline and the viscous flow did not occur, while the diameter of the nanopillars was reduced linearly with the applied fluences. Such a thinning process

was simulated and visualized via the static simulation programme TRI3DST. The sputter yields extracted from both experiments and simulation indicate an enhanced sputtering effect on the nanopillars which can be attributed to the high surface-to-volume ratio and the overlap between the collision cascade and the nanopillar surfaces. In particular the latter leads to a truncation of the collision cascade and an increasing contribution from forward sputtering to the thinning process. However, the truncation of the collision cascade in particular in the longitudinal direction increases the fraction of energy deposited in the top part of the pillar, resulting in an increase of the sputter yield in this region and ultimately leads to a reduction in height.

Compared to earlier attempts of ion beam based pillar reduction [29] our method does not require rotation of the incident direction and results in smaller final diameter. Our approach which utilizes an irradiation process at slightly elevated but still very-large-scale integration (VLSI) compatible temperatures enables new possibilities for the fabricating of vertical nanostructures, such as pillars and fins, in a top-down and CMOS-compatible manner which is not limited by the lithographic resolution.

## Acknowledgments

This work has been funded by the European Commission H-2020 programme “IONS4SET” under grant agreement No. 688072. The authors thank Roman Böttger, Ulrich Kentsch and the Ion Beam Center (IBC) at HZDR for the broad-beam irradiation.

## References

- [1] Sejoon Lee, Youngmin Lee, Emil B. Song, and Toshiro Hiramoto. Observation of Single Electron Transport via Multiple Quantum States of a Silicon Quantum Dot at Room Temperature. *Nano Letters*, 14(1):71–77, 2014.
- [2] Kevin J. Morse, Rohan J. S. Abraham, Adam DeAbreu, Camille Bowness, Timothy S. Richards, Helge Riemann, Nikolay V. Abrosimov, Peter Becker, Hans-Joachim Pohl, Michael L. W. Thewalt, and Stephanie Simmons. A photonic platform for donor spin qubits in silicon. *Science Advances*, 3(7):e1700930, 2017.
- [3] Xiaomo Xu, Thomas Prüfer, Daniel Wolf, Hans-Jürgen Engelmann, Lothar Bischoff, René Hübner, Karl-Heinz Heinig, Wolfhard Möller, Stefan Facsko, Johannes von Borany, and Gregor Hlawacek. Site-controlled formation of single



- Si nanocrystals in a buried SiO<sub>2</sub> matrix using ion beam mixing. *Beilstein journal of nanotechnology*, 9(1):2883–2892, 2018.
- [4] James W Mayer. Ion implantation in semiconductors. In *1973 International Electron Devices Meeting*, pages 3–5. IEEE, 1973.
- [5] SU Campisano, S Coffa, V Raineri, F Priolo, and E Rimini. Mechanisms of amorphization in ion implanted crystalline silicon. *Nuclear Instruments and Methods in Physics Research Section B: Beam Interactions with Materials and Atoms*, 80:514–518, 1993.
- [6] T Schuhrke, M Mändl, J Zweck, and H Hoffmann. Investigation of surface amorphization of silicon wafers during ion-milling. *Ultramicroscopy*, 41(4):429–433, 1992.
- [7] TC Pekin, FI Allen, and AM Minor. Evaluation of neon focused ion beam milling for TEM sample preparation. *Journal of microscopy*, 264(1):59–63, 2016.
- [8] Y Zhong, C Bailat, RS Averbach, SK Ghose, and IK Robinson. Damage accumulation in Si during high-dose self-ion implantation. *Journal of applied physics*, 96(3):1328–1335, 2004.
- [9] Lourdes Pelaz, Luis A. Marqués, and Juan Barbolla. Ion-beam-induced amorphization and recrystallization in silicon. *Journal of Applied Physics*, 96(11):5947–5976, 2004.
- [10] W. Wesch, E. Wendler, and C. S. Schnohr. Damage evolution and amorphization in semiconductors under ion irradiation. *Nuclear Instruments and Methods in Physics Research, Section B: Beam Interactions with Materials and Atoms*, 277:58–69, 2012.
- [11] Werner Wesch and Elke Wendler. *Ion Beam Modification of Solids*, volume 61. Springer, 2016.
- [12] Michael Anthony Nastasi and James W Mayer. *Ion implantation and synthesis of materials*, volume 80. Springer, 2006.
- [13] JS Williams. Subsurface Processing of Electronic Materials Assisted by Atomic Displacements. *Mrs Bulletin*, 17(6):47–51, 1992.
- [14] RD Goldberg, JS Williams, and RG Elliman. Amorphization of silicon by elevated temperature ion irradiation. *Nuclear Instruments and Methods in Physics Research Section B: Beam Interactions with Materials and Atoms*, 106(1-4):242–247, 1995.
- [15] Michael G Stanford, Brett B Lewis, Vighter Iberi, Jason D Fowlkes, Shida Tan, Rick Livengood, and Philip D Rack. In situ mitigation of subsurface and

- peripheral focused ion beam damage via simultaneous pulsed laser heating. *Small*, 12(13):1779–1787, 2016.
- [16] Billy L Crowder. The role of damage in the annealing characteristics of ion implanted Si. *Journal of The Electrochemical Society*, 117(5):671–674, 1970.
- [17] Ji W Mayer, L Eriksson, ST Picraux, and JA Davies. Ion implantation of silicon and germanium at room temperature. Analysis by means of 1.0-MeV helium ion scattering. *Canadian Journal of Physics*, 46(6):663–673, 1968.
- [18] F. F. Morehead and B. L. Crowder. A model for the formation of amorphous Si by ion bombardment. *Radiation Effects*, 6(1):27–32, 1970.
- [19] John R Dennis and Edward B Hale. Crystalline to amorphous transformation in ion-implanted silicon: a composite model. *Journal of Applied Physics*, 49(3):1119–1127, 1978.
- [20] Maureen L. Nietiadi, Luis Sandoval, Herbert M. Urbassek, and Wolfhard Möller. Sputtering of Si nanospheres. *Physical Review B - Condensed Matter and Materials Physics*, 90(4), 2014.
- [21] Gregor Hlawacek, Vasilisa Veligura, Raoul van Gastel, and Bene Poelsema. Helium ion microscopy. *Journal of Vacuum Science and Technology B*, 32(2):020801, March 2014.
- [22] Gregor Hlawacek and Armin Götzhäuser, editors. *Helium Ion Microscopy*. NanoScience and Technology. Springer International Publishing, Switzerland, 2016.
- [23] Wolfhard Möller. TRI3DYN–Collisional computer simulation of the dynamic evolution of 3-dimensional nanostructures under ion irradiation. *Nuclear Instruments and Methods in Physics Research Section B: Beam Interactions with Materials and Atoms*, 322:23–33, 2014.
- [24] Wolfhard Möller, Andreas Johannes, and Carsten Ronning. Shaping and compositional modification of zinc oxide nanowires under energetic manganese ion irradiation. *Nanotechnology*, 27(17), 2016.
- [25] Johannes Schindelin, Ignacio Arganda-Carreras, Erwin Frise, Verena Kaynig, Mark Longair, Tobias Pietzsch, Stephan Preibisch, Curtis Rueden, Stephan Saalfeld, Benjamin Schmid, et al. Fiji: an open-source platform for biological-image analysis. *Nature methods*, 9(7):676, 2012.
- [26] Herbert M. Urbassek, R. Mark Bradley, Maureen L. Nietiadi, and Wolfhard Möller.

- Sputter yield of curved surfaces. *Physical Review B - Condensed Matter and Materials Physics*, 91(16), 2015.
- [27] Cynthia A Volkert. Stress and plastic flow in silicon during amorphization by ion bombardment. *Journal of Applied Physics*, 70(7):3521–3527, 1991.
- [28] T Van Dillen, A Polman, CM Van Kats, and A Van Blaaderen. Ion beam-induced anisotropic plastic deformation at 300 keV. *Applied physics letters*, 83(21):4315–4317, 2003.
- [29] Andreas Johannes, Stefan Noack, Werner Wesch, Markus Glaser, Alois Lugstein, and Carsten Ronning. Anomalous Plastic Deformation and Sputtering of Ion Irradiated Silicon Nanowires. *Nano Letters*, 15(6):3800–3807, 2015.

# Supporting Information— Morphology modification of Si nanopillars under ion irradiation at elevated temperatures: plastic deformation and controlled thinning to 10 nm

Xiaomo Xu, Karl-Heinz Heinig, Wolfhard Möller, Hans-Jürgen Engelmann, Nico Klingner, Johannes von Borany and Gregor Hlawacek<sup>‡</sup>

Institute of Ion Beam Physics and Materials Research, Helmholtz-Zentrum Dresden-Rossendorf, Bautzner Landstrasse 400, 01328 Dresden, Germany

Ahmed Gharbi, Raluca Tiron

CEA-Leti, Rue des Martyrs 17, 38054 Grenoble, France

E-mail: g.hlawacek@hzdr.de

## 1 Ne<sup>+</sup> amorphization of nanopillars

Figure S1 shows energy-filtered transmission electron microscopy (EFTEM) and bright-field transmission electron microscopy (BF-TEM) micrographs of nanopillars irradiated at (a-b) 275 °C and (c-d) 325 °C with 25 keV Ne<sup>+</sup> of  $2 \times 10^{16} \text{ cm}^{-2}$  fluence. By comparing the EFTEM and BF-TEM images it is clear that the majority of a nanopillar after the irradiation at 275 °C is amorphous while nearly the entire nanopillar after the irradiation at 325 °C remains crystalline. Together with Figure 2 we conclude that the critical temperature of amorphization in this case is slightly higher than 325 °C.

## 2 Experimental measurement of the sputter yield

The sputter yield on a nanopillar can be calculated via a series of EFTEM micrographs of originally identical nanopillars after different fluencies. According to the definition, the sputter yield is calculated by dividing the total number of sputtered atoms ( $N_{\text{sputter}}$ ) with the total number of ion hitting the nanopillar ( $N_{\text{ion}}$ ). Figure S2 shows an example

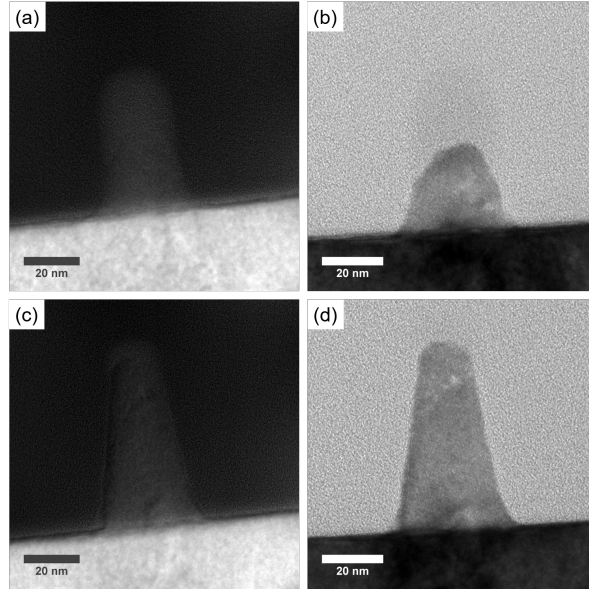


Figure S1: EFTEM and BF-TEM micrographs show nanopillars irradiated at (a-b) 275 °C and (c-d) 325 °C with 25 keV Ne<sup>+</sup> of  $2 \times 10^{16} \text{ cm}^{-2}$  fluence. The majority of a nanopillar structure irradiated at 275 °C is amorphous while almost the entire nanopillar after the irradiation at 325 °C remains crystalline.

to measure  $N_{\text{sputter}}$  and  $N_{\text{ion}}$  with an original nanopillar, the same procedure was applied to nanopillars irradiated with varied fluences.

The nanopillar is imaged with EFTEM at 17 eV plasmon-loss peak (a) and the micrograph is rotated and cropped according to the shape of the nanopillar (b). Although the nanopillar has an irregularly tapered sidewall, at any certain height the horizontal cross-section is taken as circular. As shown in Figure S2(c), a Minimum Error threshold [1] is applied to distinguish the Si elemental contrast of the nanopillar from the background. In Figure S2(d) a mesh with  $5 \text{ nm}^2$  grid is overlaid and the diameter at each height can be measured. Thus, the volume of a nanopillar can be approximately calculated by summing up the volume of all conical segments, and the sputtered atom number  $N_{\text{sputter}}$  in each fluence interval can be calculated by multiplying the volume difference and the atomic density of Si ( $50 \text{ atoms/nm}^3$ ).

The number of incident ions  $N_{\text{ion}}$  can be obtained by multiplying the fluence interval with the nanopillar cross-section. The diameter used for the cross-section calculation is taken as the half-height diameter to be consistent with the pillar thinning process in Figure 3 and Figure 5.

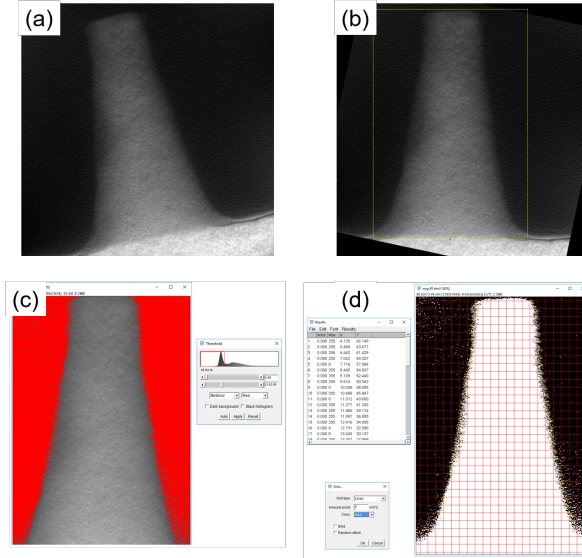


Figure S2: (a) An EFTEM micrograph shows a Si nanopillar before ion irradiation. After the image is rotated and cropped (b), a Minimum Error threshold is applied to distinguish the Si elemental contrast from the background. A mesh grid with the density of  $5 \text{ nm}^2$  is overlaid on the nanopillar and the diameter and volume of a nanopillar can be measured.

### 3 Computer Simulations

For ballistic simulations of the scattering of impinging ions from the irradiated structure, their slowing down in the material and the effects of the associated collision cascades such as damage formation and surface sputtering, static TRI3DST [2, 3] and dynamic TRI3DYN [4, 5] codes have been employed which make use of the binary collision approximation (BCA). Their collisional algorithms, being valid for amorphous materials, are based on early static [6, 7] and dynamic [8, 9] versions of the widely spread TRIM code [10]. Briefly, the simulations trace the trajectories of incident ions and recoil atoms, which are generated in the associated collision cascades by binary atomic interactions in a screened Coulomb potential with the  $Kr-C$  parametrization [11]. Energy transfer to the target electrons is modeled by an equipartition of local [12] and nonlocal [13] energy losses. The results addressing surface sputtering and bulk atomic displacement depend on the preselected parameters of the surface binding energy and the displacement threshold energy, respectively. For the former, the standard selection of the sublimation enthalpy of  $4.7 \text{ eV}$  for Si results in flat-surface sputtering yields which agree well with experimental data [14]. The definition of the displacement threshold energy is less straightforward. Tabulated data are available for crystalline materials at low damage

levels [15–17]. However, most materials are highly damaged under ion irradiation at high fluences and sufficiently low temperatures. Under the conditions of the present work, Si becomes amorphized already at fluences which are much smaller than the ones employed here. Then, displacements may occur at lower energies due to trapping at preexisting defects. In their pioneering theoretical paper on ion mixing, Sigmund and Gras-Marti [18] propose a threshold energy of 7.8 eV for cascade mixing in Si. In consistence with this choice, a default setting of  $U_d=8$  eV has been successful in numerous ion mixing, preferential sputtering and thin film deposition studies using TRIDYN [19] and is also applied here.

In TRI3DST, a variety of three-dimensional bodies can be selected, which are defined by analytical functionals describing their surface. For the present paper (see Figure 4), conical Si nanopillars are irradiated in the direction along the pillar axis by a nanobeam with a Gaussian beam profile of 3 nm full-width at half maximum. For clarity of the extracted distributions of sputter ejection sites at simultaneously reasonable statistics, 1000 incident ions have been traced in each run.

TRIDYN works with a fixed 3D grid of cuboidal voxels which span a cuboidal computational volume. On the voxel grid, arbitrary initial structures can be defined and their modification of the local bulk composition and surface contour during irradiation can be traced. For the present simulations (see Figures 2 and 3), tapered Si nanopillars of 70 nm height and upper/lower diameters of 19/29 nm (see Figure 2) and 42/56 nm (see Figure 3) have been set up on a planar Si substrate with voxel dimensions of  $0.8 \times 0.8 \times 0.8$  nm<sup>3</sup> and  $1 \times 1 \times 1$  nm<sup>3</sup>, respectively. Periodic boundaries are applied in the directions normal to the pillar axes. Laterally uniform irradiation is accomplished with the ions starting at randomly selected positions on the upper plane of the computational volume. For the entry of ions at glancing incidence (in particular at the tapered flanks of nanopillars), the voxel structure may result in an artificially enhanced entry and trapping, whereas in reality such ions would be preferentially reflected from the wall [4]. Consequently, an algorithm of 3D surface planarization has been developed which replaces the cuboidal surface of each surface voxel by a locally planar surface with an inclination taking into account the neighboring surface voxels.

The ballistic transport of incident projectiles or recoil atoms generated in the collision cascades may remove atoms from specific voxels due to bulk displacements or surface sputtering, or add displaced atoms or slowed-down projectiles. (The incorporation of Ne projectiles is neglected in the present simulations as its contribution

to the local atomic densities is negligible in the present range of ion fluence.) For the dynamic relaxation of the structure during irradiation, each moving atom (*pseudoatom*) in the simulation represents a certain number of real atoms, which may be fractional (0.25 and 1.0 for the present cases of Figure 2 and Figure 3, respectively), and which is automatically chosen to minimize the computation time at still sufficient statistical quality of the dynamic development of the system. After a certain number of incident pseudoprojectiles each, the dynamic relaxation of the system is activated. In each modified bulk voxel, the atomic density is re-established. This is accomplished by material exchange between neighboring voxels and transport from/to surface voxels (for details, see Ref. [4]). Surface voxels which are depleted due to sputtering are combined and partially turned into vacuum voxels. Each relaxation procedure is terminated by an algorithm of surface smoothing.

## Acknowledgments

This work has been funded by the European Commission H-2020 programme “IONS4SET” under grant agreement No. 688072. The authors thank Roman Böttger, Ulrich Kentsch and the Ion Beam Center (IBC) at HZDR for the broad-beam irradiation.

## References

- [1] Josef Kittler and John Illingworth. Minimum error thresholding. *Pattern recognition*, 19(1):41–47, 1986.
- [2] Maureen L. Nietiadi, Luis Sandoval, Herbert M. Urbassek, and Wolfhard Möller. Sputtering of Si nanospheres. *Physical Review B - Condensed Matter and Materials Physics*, 90(4), 2014.
- [3] Herbert M. Urbassek, R. Mark Bradley, Maureen L. Nietiadi, and Wolfhard Möller. Sputter yield of curved surfaces. *Physical Review B - Condensed Matter and Materials Physics*, 91(16), 2015.
- [4] Wolfhard Möller. Tri3dyn–collisional computer simulation of the dynamic evolution of 3-dimensional nanostructures under ion irradiation. *Nuclear Instruments and Methods in Physics Research Section B: Beam Interactions with Materials and Atoms*, 322:23–33, 2014.
- [5] Wolfhard Möller, Andreas Johannes, and Carsten Ronning. Shaping and



- compositional modification of zinc oxide nanowires under energetic manganese ion irradiation. *Nanotechnology*, 27, 2016.
- [6] Jochen P Biersack and LG Haggmark. A monte carlo computer program for the transport of energetic ions in amorphous targets. *Nuclear Instruments and Methods*, 174(1-2):257–269, 1980.
- [7] JP Biersack and W Eckstein. Sputtering studies with the monte carlo program trim. sp. *Applied Physics A*, 34(2):73–94, 1984.
- [8] W Möller and W Eckstein. Tridyna trim simulation code including dynamic composition changes. *Nuclear Instruments and Methods in Physics Research Section B: Beam Interactions with Materials and Atoms*, 2(1-3):814–818, 1984.
- [9] Wolfhard Möller, Wolfgang Eckstein, and JP Biersack. Tridyn-binary collision simulation of atomic collisions and dynamic composition changes in solids. *Computer Physics Communications*, 51(3):355–368, 1988.
- [10] James F Ziegler, Matthias D Ziegler, and Jochen P Biersack. Srim—the stopping and range of ions in matter (2010). *Nuclear Instruments and Methods in Physics Research Section B: Beam Interactions with Materials and Atoms*, 268(11-12):1818–1823, 2010.
- [11] WD Wilson, LG Haggmark, and JP Biersack. Calculations of nuclear stopping, ranges, and straggling in the low-energy region. *Physical Review B*, 15(5):2458, 1977.
- [12] Ordean S Oen and Mark T Robinson. Computer studies of the reflection of light ions from solids. *Nuclear instruments and Methods*, 132:647–653, 1976.
- [13] J Lindhard and M Scharff. Energy dissipation by ions in the kev region. *Physical Review*, 124(1):128, 1961.
- [14] Wolfgang Eckstein and Herbert M Urbassek. Computer simulation of the sputtering process. In *Sputtering by Particle Bombardment*, pages 21–31. Springer, 2007.
- [15] HH Andersen. The depth resolution of sputter profiling. *Applied physics*, 18(2):131–140, 1979.
- [16] D Marton and JW Rabalais. Low energy ion-surface interactions. *by JW Rabalais (John Wiley & Sons, Chichester, 1994) p*, 488, 1994.
- [17] SJ Zinkle and C Kinoshita. Defect production in ceramics. *Journal of Nuclear Materials*, 251:200–217, 1997.

- [18] Peter Sigmund and A Gras-Marti. Theoretical aspects of atomic mixing by ion beams. *Nuclear Instruments and Methods*, 182:25–41, 1981.
- [19] Wolfhard Möller and Matthias Posselt. Tridyn fzf user manual. *Wissenschaftlich-Technische Berichte Forschungszentrum Rossendorf*, FZR-317, 2001.